Spring 2018

# Understanding the Nature of Nanoscale Wetting Through All-Atom Simulations

Oliver Evans
oge1@zips.uakron.edu

Please take a moment to share how this work helps you through this survey. Your feedback will be important as we plan further development of our repository.
Follow this and additional works at: http://ideaexchange.uakron.edu/honors_research_projects

Part of the Atomic, Molecular and Optical Physics Commons, Numerical Analysis and Computation Commons, and the Ordinary Differential Equations and Applied Dynamics Commons

UNDERSTANDING THE NATURE OF NANOSCALE WETTING THROUGH

ALL-ATOM SIMULATIONS

A Honors Research Project

Presented to

The Honors College of The University of Akron

In Partial Fulfillment

of the Requirements for the Degree

Bachelor of Science with Honors

Oliver Graham Evans

May, 2018

# UNDERSTANDING THE NATURE OF NANOSCALE WETTING THROUGH

# ALL-ATOM SIMULATIONS

Oliver Graham Evans

Department of Mathematics

Honors Research Project

submitted to: The Honors College

Approved:                                    Accepted:

_____                      _____  4/27/18
Honors Project Sponsor    Date               Department Chair          Date
Dr. Mesfin Tsige                             Dr. Kevin Kreider

_____  4/26/2018           _____  4/27/2018
Faculty Reader            Date               Honors Faculty Advisor    Date
Dr. Malena Español                           Dr. Curtis Clemons

_____  4/27/2018           _____
Faculty Reader            Date               Dean, Honors College      Date
Dr. Pat Wilber                               Dr. Sarah M.R. Cravens

ii

# ABSTRACT

The spreading behavior of spherical and cylindrical water droplets between 30Å and 100Å in radius on a sapphire surface is investigated using all-atom molecular dynamics simulations for durations on the order of tens of nanoseconds. A monolayer film develops rapidly and wets the surface, while the bulk of the droplet spreads on top of the monolayer, maintaining the shape of a spherical cap. Unlike previous simulations in the literature, the bulk radius is found to increase to a maximum value and receed as the monolayer continues to expand. Simple time and droplet size dependence is observed for monolayer radius and contact angle, and a mathematical model for the spreading dynamics is developed to predict droplet height and bulk radius over time. The model predictions match the simulation data reasonably well, although more work remains in understanding the distinct temporal regimes in the wetting process which this work does not consider.

I would like to express my deep gratitude for my friends, family, and community who have supported me throughout my education. Without the love, the science would not feel worthwhile.

TABLE OF CONTENTS

# LIST OF TABLES

LIST OF FIGURES

CHAPTER I

INTRODUCTION

Water is one of the most abundant substances on Earth, and it plays a crucial role in countless aspects of human society. As a ubiquitous example, wetting is the driving process behind corrosion, which is estimated to cost $2.5 trillion globally per year across a wide variety of industries [7]. Wetting also leads to icing, which in many cases, such as airplane wings and wind turbines, can create significant safety hazards and operational inefficiencies [15, 11]. Furthermore, understanding the nature of wetting is fundamental to optimizing the design and application of coatings which can be applied to alter surface properties of materials [14].

Wetting has been studied for hundreds of years, dating back to the work of Young and Laplace in the eighteenth and nineteenth centuries [5]. Several models have been developed to describe wetting, most importantly the hydrodynamic model and the molecular-kinetic model. The hydrodynamic model takes the classical fluid mechanics approach of describing the droplet as a continuous fluid. However, the traditional no-slip boundary condition fails in the case of a spreading droplet, leading to infinite dissipation near the edge of the droplet [6], leading to the development of alternate boundary conditions permitting interfacial slipping. Meanwhile, the molecular-kinetic model takes a statistical mechanics approach, treating the liquid-

1

solid-vapor interface as a zone of finite width where the three phases meet, rather than an infinitesimal line [2].

These models differ in their prediction of certain aspects of the wetting dynamics. For example, the molecular-kinetic model predicts that the bulk radius of the droplet has a $t^{1/7}$ dependence, whereas the hydrodynamic model predicts the bulk radius to expand as $t^{1/10}$ [6]. While many predictions of of the theory can be verified against experimental evidence, the experimentalists face significant constraints in terms of what can be measured, what time and length scales are feasible to be studied, and which parameters can be controlled. Computer simulations, on the other hand, are extraordinarily flexible in the degree to which it is possible to control parameters and extract useful information. In all-atom simulations specifically, the position and velocity of every atoms is calculated over time. From this raw data, nearly any other macroscopic quantity of interest can be calculated. All-atom simulations are also limited in their feasible length scales, however they are limited from above whereas experimentalists studying microscopic quantities are limited from below. As increasingly powerful hardware and algorithms are developed, the upper limits of length and time scales can be extended. This type of simulation can therefore be used in a growing number of applications to bridge the gap between theory and experiment in the search for deeper understanding of fundamental physics.

As a computational contribution to the study of wetting, we perform all-atom simulations of spherical and cylindrical water droplets on the order of of several nanometers in radius for time scales on the order of tens of nanoseconds in duration,

using sapphire as a substrate. Where feasible, we study the full wetting process for spherical droplets, whereas others have focused primarily on the earlier stages [9, 4]. However, the cylindrical droplets are found to wet very slowly, since they spread in only one dimension, whereas the spherical droplet spreads in two, causing them to take up to an order of magnitude longer to completely wet the substrate.

Our emphasis in this work is on the dynamics of the droplet geometry during the wetting process. In simulations presented, the formation of a monolayer of water, a liquid film only a single molecule thick, is observed. While the monolayer wets the surface rapidly, the bulk of the droplet retains the shape of a spherical cap, spreading at a slower rate on to the surface which has already been wet by the monolayer. The time dependence and droplet size dependence of the radius of the bulk and monolayer are studied, in addition to the bulk droplet height and the contact angle which the bulk makes with the monolayer.

The rest of this document is organized as follows. In Chapter 2, we discuss simulation details and explain the algorithm used to calculate the geometrical features of interest from the raw data. In Chapter 3, we review the power law relationships found in the time series data of the extracted features, and demonstrate the linear dependence of these power laws on droplet size. In Chapter 4, we introduce a mathematical model which uses the results of the previous chapter along with the assumption of minimal evaporation in order to predict the time-dependence of those features extracted from the data which did not exhibit easily identifiable behavior. In Chapter 5, we summarize our results and give concluding remarks.

# CHAPTER II

# SIMULATION AND FEATURE EXTRACTION

## 2.1 Molecular Dynamics Simulation
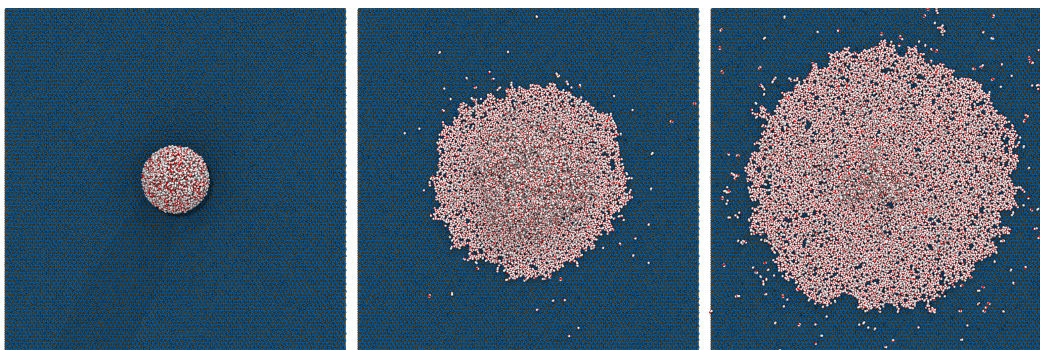


Figure 2.1: Spherical 40 Å droplet at 0 ns, 2 ns, and 10 ns, top view.
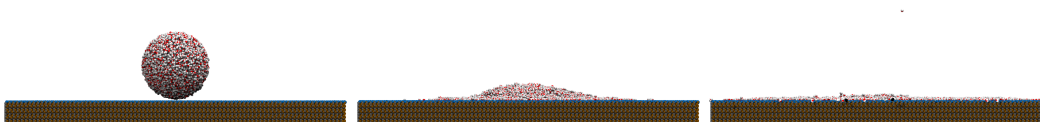


Figure 2.2: Spherical 40 Å droplet at 0 ns, 2 ns, and 10 ns, side view.

All-atom simulations of spherical and cylindrical water droplets on sapphire are performed using LAMMPS, the open source molecular dynamics package from Sandia National Lab [12]. We simulate spherical and cylindrical droplets using the SPC/E

water force field [1], and a sapphire substrate using the CLAYFF force field [3]. For the spherical droplets, we use a $400\,\text{Å} \times 400\,\text{Å}$ square substrate, and droplets of radius 30Å, 40Å, 50Å, and 60Å, with periodic boundary conditions in each dimension. Complete wetting is achieved for the $30\,\text{Å}$ and $40\,\text{Å}$ can undergo complete wetting on this size substrate without significant interaction with their periodic image. For the $50\,\text{Å}$ and $60\,\text{Å}$ droplets, however, only partial wetting can be studied due to the size limitations of the substrate.
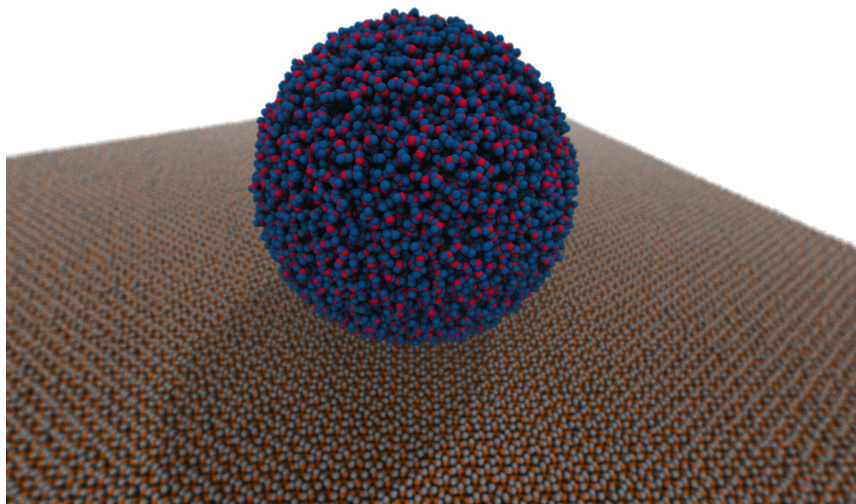


Figure 2.3: Spherical droplet geometry

The cylindrical droplets require a smaller substrate, as they extend along the full $y$ axis, which is their symmetry axis, and the spreading occurs only in the $x$ direction. Therefore, we use a $950\,\text{Å} \times 100\,\text{Å}$ substrate, and cylindrical droplets of radius 40Å, 50Å, and 100Å. Since the stability of cylindrical droplets depends on their infinite extent, they do not exist in nature, per se. However, they are commonly
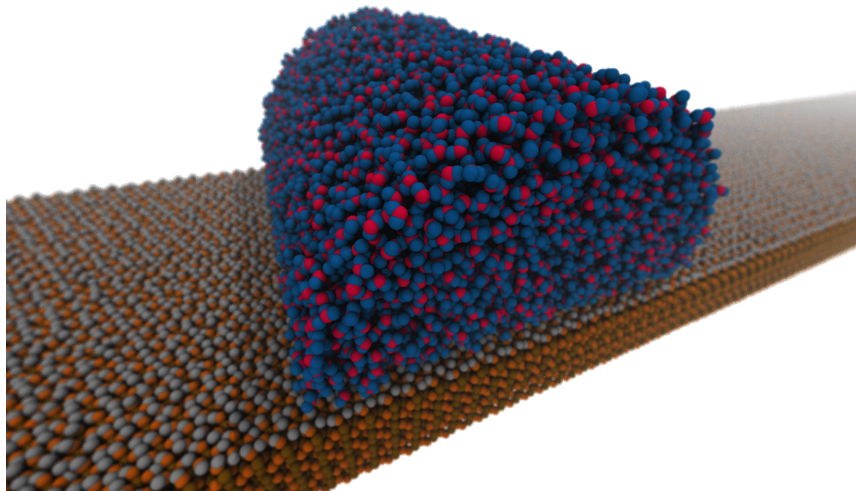
Figure 2.4: Cylindrical droplet geometry

used in computation because of the reduced the number of atoms required [8, 13, 9].
We have observed, however, that the timescales required to simulate full wetting are
often orders of magnitude longer than a similar size spherical droplet, more than
offsetting any savings due to reducing the number of atoms. It seems, then, that
while cylindrical droplets may be a useful tool for studying the early stages of wetting,
they are not well suited for studies of total wetting.

As an example to give an idea of the computational time required for these
simulations, about 32 days running on 120 processors distributed over 5 computa-
tional nodes to simulate $20\,\mathrm{ns}$ of the $40\,\text{Å}$ cylindrical droplet. For the $50\,\text{Å}$, the
same simulation duration would take approximately 2 months on 144 processors
distributed over 6 nodes.

| Geometry | Substrate size | # substrate atoms | Droplet radius | # water atoms |
|----------|----------------|-------------------|----------------|---------------|
| Spherical | 400 Å × 400Å | 500,000 | 20 Å - 60Å | 3,000 - 80,000 |
| Cylindrical | 950 Å × 100Å | 320,000 | 50 Å - 100Å | 40,000 - 170,000 |

Table 2.1: Simulation details

## 2.2 Extraction of Geometrical Features

Once the simulation is complete, we have the positions of all atoms at each time step. Before drawing any useful conclusions, we must first extract the relevant quantities. As mentioned, the formation of a monolayer film is observed which wets the surface, while the bulk of the droplet maintains the shape of a spherical cap and spreads on to the monolayer. The specific geometric quantities of interest to us are the monolayer radius $r_m$, the bulk radius $r_b$, the bulk height $h_m$, and the contact angle $\theta$. To determine these quantities, we create a spatial density histogram and perform curve fitting to determine the droplet boundary [6]. A brief description of this boundary detection algorithm follows.

### 2.2.1 Droplet boundary detection

For the spherical droplets, we begin by assuming azimuthal symmetry, that is, symmetry with respect to the $z$ axis. We can then create a two-dimensional histogram in cylindrical coordinates with radius $r$ in the $x$-$y$ plane on one axis, and vertical height $z$ on the other. We break the $r$-$z$ domain into discrete rectangular bins of

*equal area* in the $r$-$z$ plane (which ensures equal volume for each bin), and calculate the density of the atoms in each bin. We choose bins of equal volume rather than choosing an even $r$ spacing so that the number of atoms in each bin is approximately equal, leading to a uniform accuracy in the density calculation in all bins. Note that each bin in the $r$-$z$ plane is a rectangle revolved around the $z$ axis, effectively averaging density over azimuthal angle.
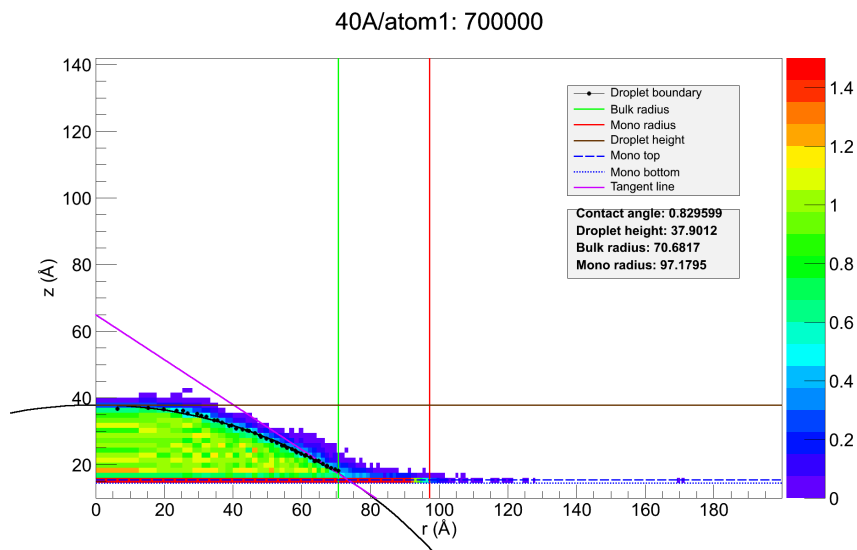


Figure 2.5: 2D Density Histogram

Once we have this rectangular grid of density values, we consider each row and column separately. In both directions, we expect that the density is approximately constant over the bulk of the droplet, and decreases smoothly to zero at the boundary. Since the bulk volume of water is $1\,\mathrm{g/cm^3}$, we consider the edge of the droplet to be the position where the density is $0.5\,\mathrm{g/cm^3}$, that is, half way between the vacuum density and bulk density. To obtain this location, we consider a shifted

hyperbolic tangent curve of the form

$$\rho(r) = \frac{\rho_m}{2}\left(1 - \tanh\left(4\frac{r - r_0}{w}\right)\right). \tag{2.1}$$

For each row and column of density values in the grid, we explicitly calculate the position where this curve has the desired edge density.
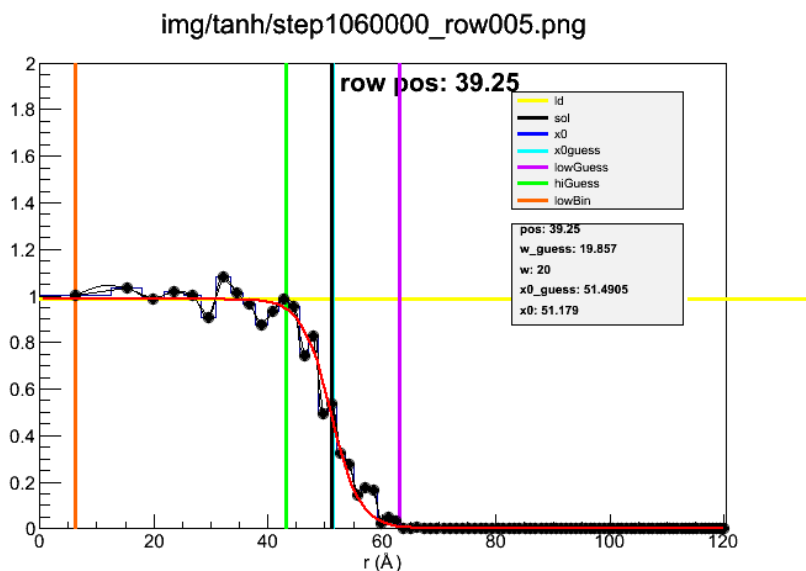


Figure 2.6: Hyperbolic tangent fit to one row of density values

2.2.2   Spherical Cap Fitting

After calculating the edge location along each row and column in the $r$-$z$ grid, we perform one more round of curve fitting. We mirror the points about the $z$ axis and calculate the circle of best fit in the $r$-$z$ plane. Then, the portion of the circle in the first quadrant is rotated about the $z$ axis to generate the spherical cap which approximates the surface of the bulk of the droplet. Generating this surface allows

9

us to easily calculate the droplet height $h_b$, the base radius $r_b$, and the contact angle $\theta$ with the top of the monolayer as follows.

Let the fitted circle in the $r$-$z$ plane have the equation $r^2 + (z - z_0)^2 = R^2$, let the top of the monolayer be located at $z = h_m$, and let $\varphi = \pi - \theta$. Then,

$$\cos\theta = \cos(\pi - \varphi) = -\cos\varphi. \tag{2.2}$$

From Figure 2.7, we observe the following relationships which allow us to calculate the geometrical properties of interest.

$$\theta = \cos^{-1}\left(\frac{z_m - z_0}{R}\right) \tag{2.3}$$

$$r_b = \sqrt{R^2 - (h_m - z_0)^2} \tag{2.4}$$

$$h_b = R - h_m + z_0 \tag{2.5}$$
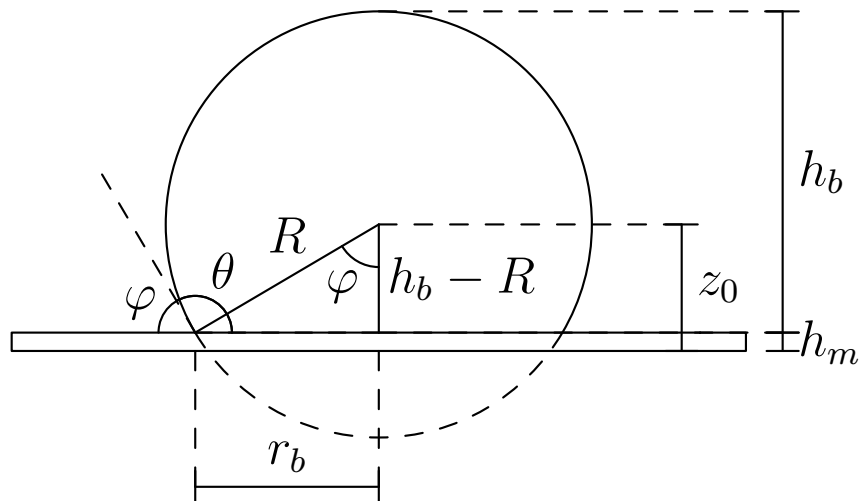


Figure 2.7: Droplet geometry

10

For the cylindrical droplets, the boundary determination procedure is identical except that rectangular Cartesian grids are used, the $y$ position of atoms is averaged over, and the two-dimensional histogram exists in the $x$-$z$ plane instead of the $r$-$z$ plane.
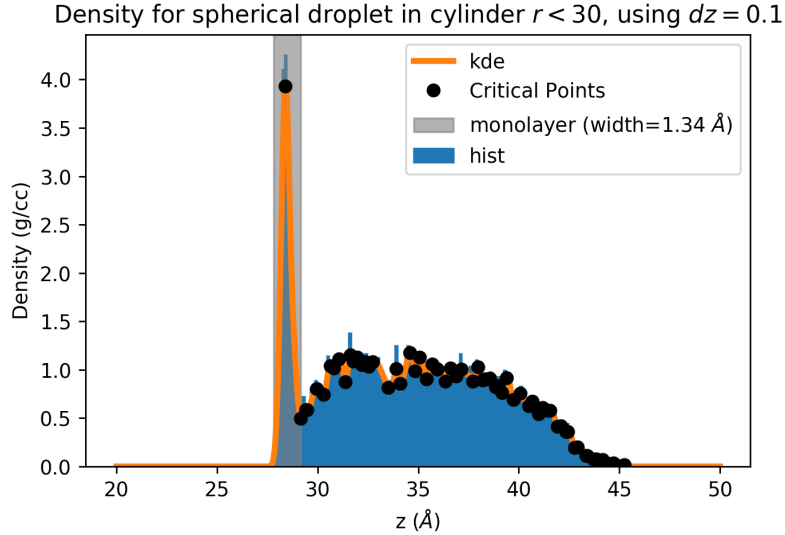


Figure 2.8: Water density as a function of vertical position

We also calculate the radius of the monolayer using a similar procedure as described above for the row and column fitting curves. Note that in Figure 2.8, the monolayer can be distinguished from the bulk by its significantly higher density $\rho_m$. A $z$ slab can be determined for the monolayer, and all atoms within that slab are combined into a single histogram row which is then used to calculate the monolayer density as a function of distance from the $z$ axis. Then, the monolayer radius is defined to be the distance at which the monolayer density is $\rho_m/2$.

### 2.2.3  Monolayer Density Calculation

The algorithm used here to determine the extent and density of the monolayer is as follows. A cylindrical radius is chosen which is known to be smaller than the bulk radius (in the figure, $r = 30$Å is used). A kernel density estimate (KDE) is constructed by representing each atom in that cylinder by a one-dimensional Gaussian in the $z$ dimension and summing to create a density profile for the droplet as a whole. The KDE is in some sense the continuous analogue of a histogram, and the chosen width of each Gaussian is similar to the width of each histogram bin. In general, this width should be chosen to be as small as possible without introducing excessive high-frequency noise into the density profile. In the above figure, a Gaussian width of $0.1$ Å is used. We expect to observe a single peak followed by a slight dip indicating the end of the monolayer. Therefore, we calculate critical points of the KDE are then numerically. The first critical point is the center of the monolayer, and the second is the top of the monolayer.

Then, the distance between the first nonzero value and the second critical point in the KDE is $h_m$, the monolayer height. By integrating the density profile over this interval and dividing by the monolayer height, we arrive at $\rho_m$, the average density of water in the monolayer. By repeating this procedure for several time steps and averaging over them, we found that on average, $\rho_m = 1.5$ g/cm$^3$ and $h_m = 1.75$ Å for all droplet sizes.

CHAPTER III

OBSERVATIONS FROM SIMULATION DATA

The following results are produced from the analysis procedure described in Section 2.2. The monolayer radius is found to obey the simple power law $r_m(t) = \alpha t^\beta$ for both the spherical and cylindrical droplets. The contact angle for the cylindrical droplets appears to decrease as $\theta(t) = at^{-b}$, whereas for the spherical droplets, the contact angle asymptotic to a nonzero value, $\theta_\infty$, according to the relationship $\theta(t) = \theta_\infty + at^{-b}$. Of course, at the very last stage of wetting, there is no longer a well defined spherical bulk, and only the monolayer remains, at which time the contact angle is zero. It is important to note that the data presently available for the cylindrical droplets comprises a very small portion of the overall wetting process, and therefore these preliminary trends may not be accurate. For example, perhaps the cylindrical droplets do, in fact, tend towards a nonzero contact angle. This is not yet clear from the data, and it is highly recommended that these cylindrical simulations be run further and for these observations to be reconsidered after they are complete. The bulk radius and droplet height do not show easily describable trends, and are discussed in Chapter 4.

In the following sections, we show the results of curve fitting using a least squares approach to extract these power law parameters from the data. Through

experimentation not shown here, we observe that the power law exponents are constant for all droplet sizes, and therefore they are held constant during fitting with the values Note that most of the curve fits are more accurate at later times. It is clear that there are multiple qualitatively different temporal regimes in the wetting process. The investigation of these regimes is recommended for future work.

$$\beta^{\mathrm{sph}} = 0.2, \tag{3.1}$$

$$b^{\mathrm{sph}} = 0.5, \tag{3.2}$$

$$\beta^{\mathrm{cyl}} = 0.25, \tag{3.3}$$
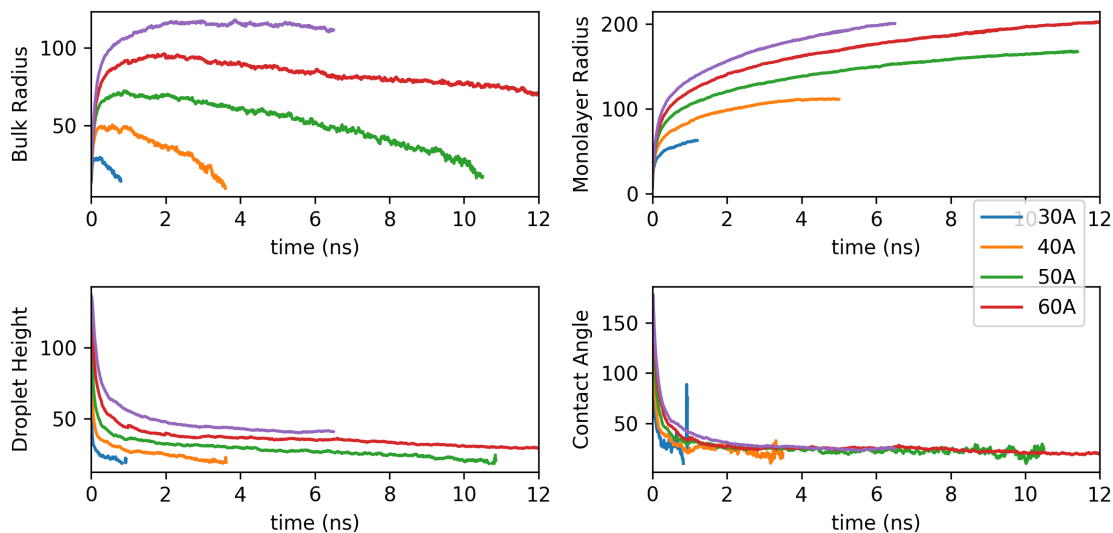
$$b^{\mathrm{cyl}} = 0.25. \tag{3.4}$$



Figure 3.1: Spherical wetting dynamics

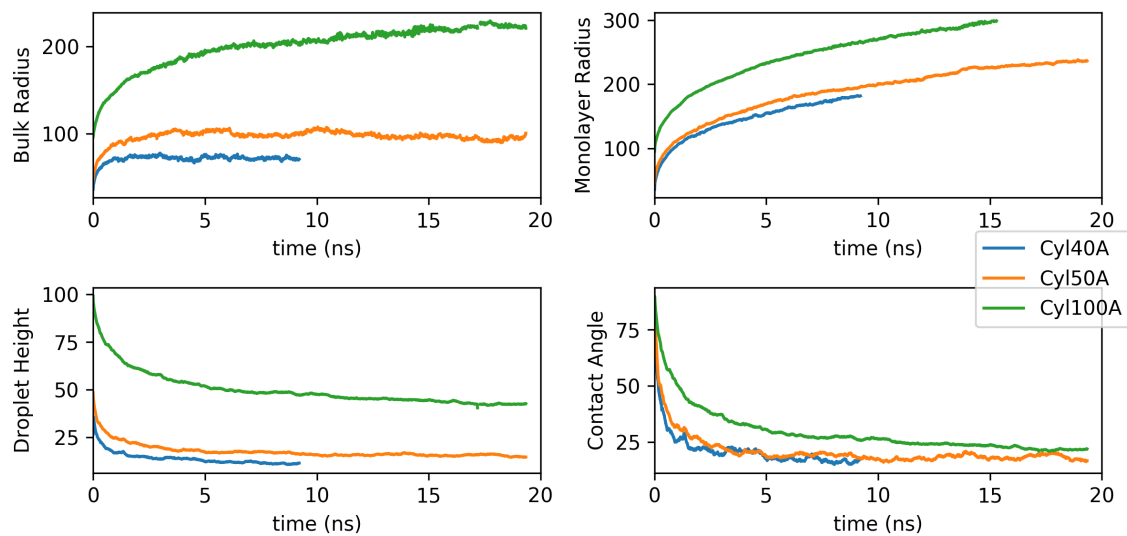Figure 3.2: Cylindrical wetting dynamics

## 3.1 Spherical Fitting Curves



Figure 3.3: Spherical monolayer radius fitting curves

Figure 3.4: Spherical monolayer radius fitting curves (log)



Figure 3.5: Spherical contact angle fitting curves
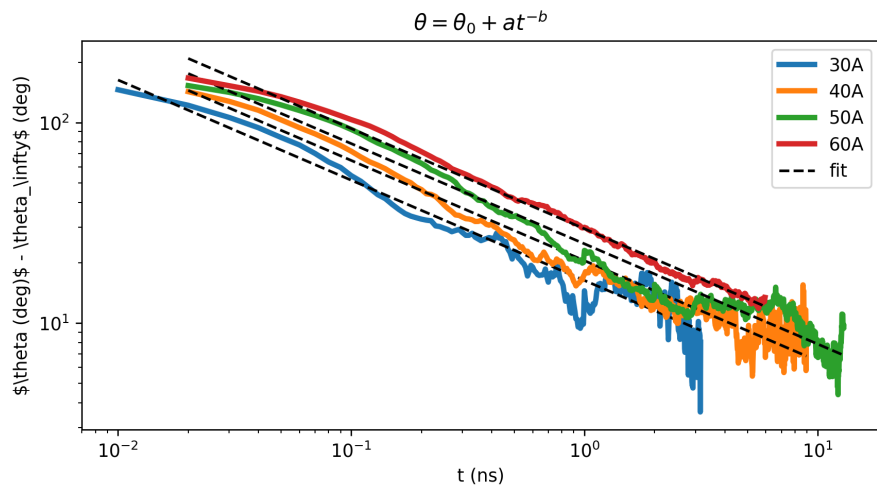
Figure 3.6: Spherical contact angle fitting curves (log)

## 3.2 Cylindrical Fitting Curves
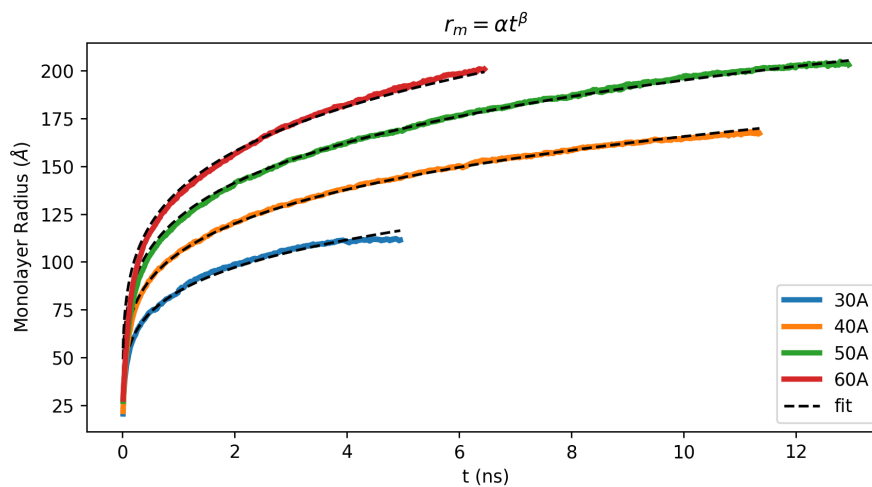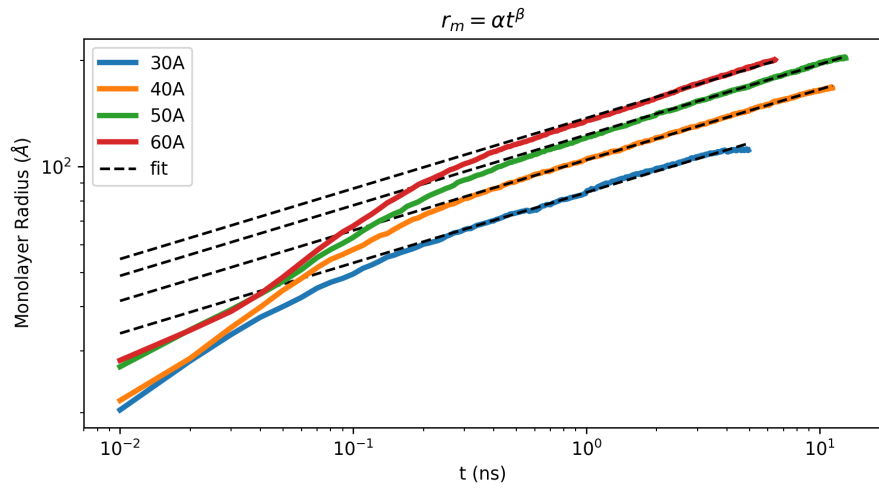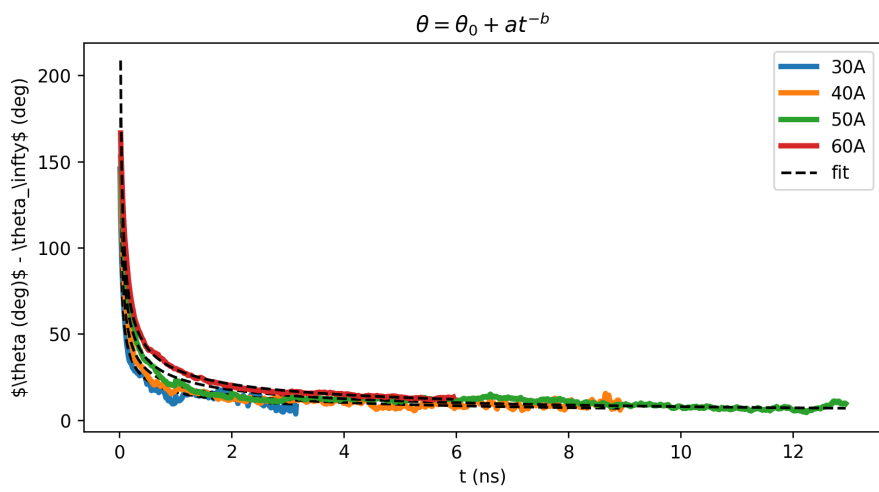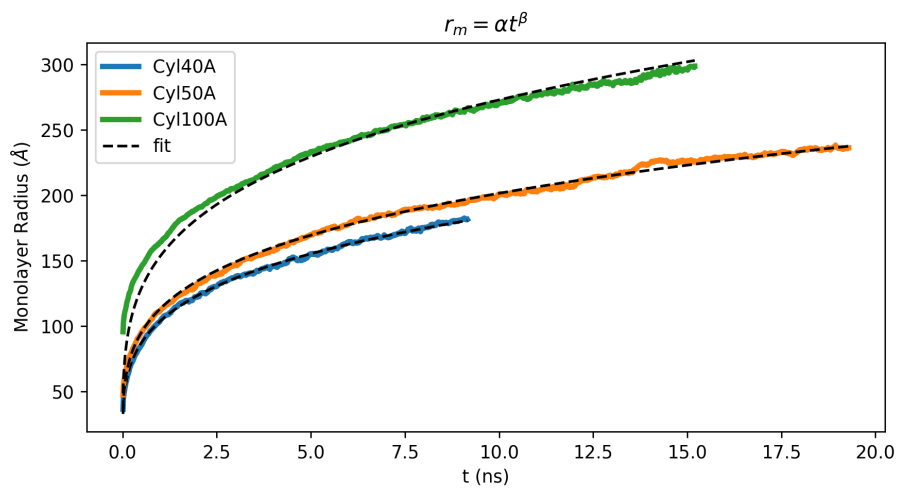


Figure 3.7: Cylindrical monolayer radius fitting curves
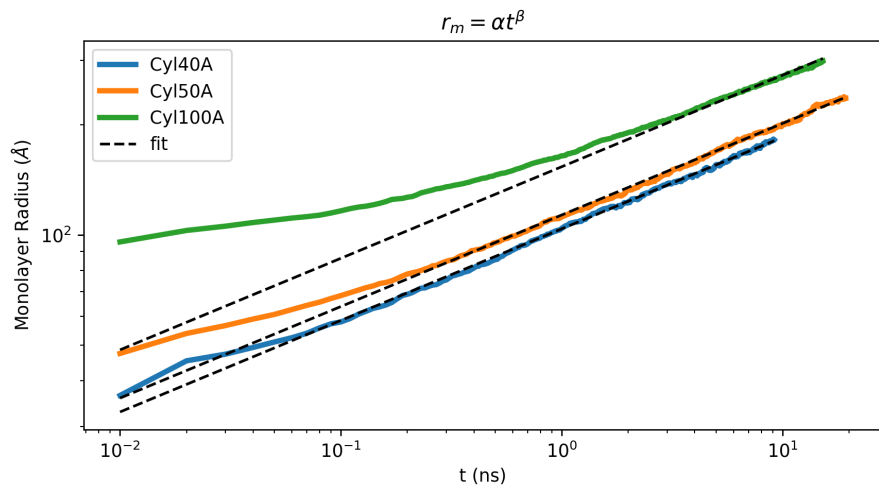
Figure 3.8: Cylindrical monolayer radius fitting curves (log)
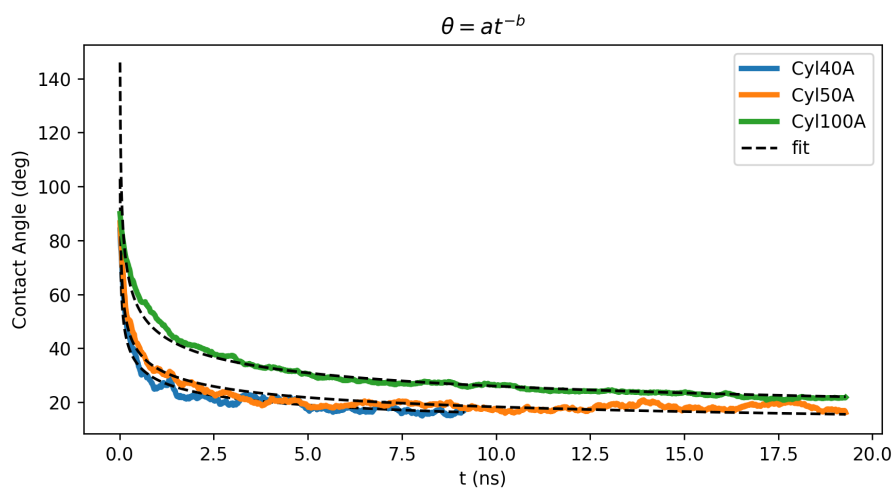


Figure 3.9: Cylindrical contact angle fitting curves
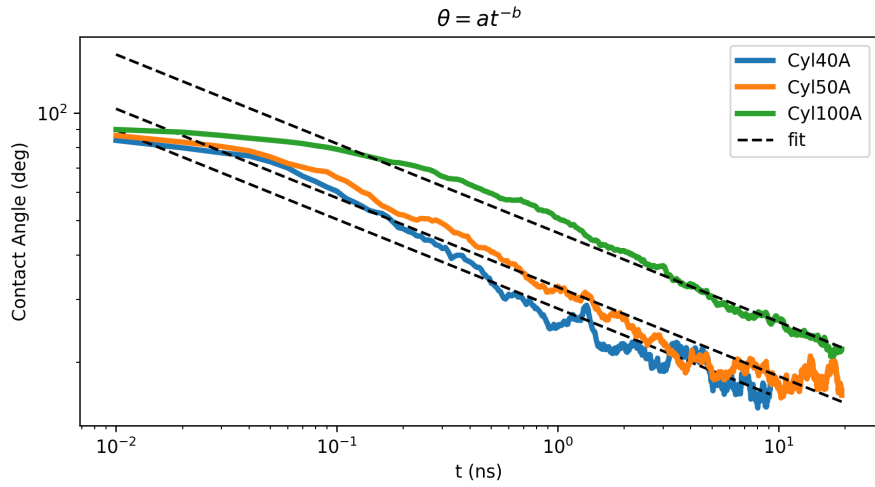
Figure 3.10: Cylindrical contact angle fitting curves (log)

## 3.3 Droplet Size Dependence of Fitting Curves

We observe simple linear relationships between all curve fitting parameters, which are detailed below. These simple relationships allow for the estimation of the power law behavior of other droplet sizes not yet simulated. In Chapter 4, these power laws will be used to model $r_b$ and $h_b$. These linear relationships allow this model to be used predictively to estimate the wetting dynamics of a droplet size for which the full all-atom simulation has not been performed.

### 3.3.1   Spherical



Figure 3.11: Droplet size dependence of $\alpha$ for spherical droplets from $r_m(t) = \alpha t^\beta$, with $\beta = 0.2$.



Figure 3.12: Droplet size dependence of $\alpha$ for spherical droplets from $\theta(t) = \theta_\infty + at^b$, with $b = 0.5$.

Figure 3.13: Droplet size dependence of $\theta_\infty$ for spherical droplets from $r_m(t) = \alpha t^\beta$, with $\beta = 0.2$.

| Droplet Size | $\alpha$ | $\theta_\infty$ | $a$ |
|---|---|---|---|
| 30Å | 84.49 | 10.94 | 16.29 |
| 40Å | 104.48 | 13.49 | 20.45 |
| 50Å | 123.07 | 13.10 | 24.82 |
| 60Å | 137.34 | 10.99 | 29.51 |

$$\alpha^{\text{sph}} = 1.77 R_0 + 32.64 \tag{3.5}$$

$$a^{\text{sph}} = 0.44 R_0 + 2.97 \tag{3.6}$$

$$\theta_\infty^{\text{sph}} = 12.24 \tag{3.7}$$

Table 3.1: Spherical fit coefficients
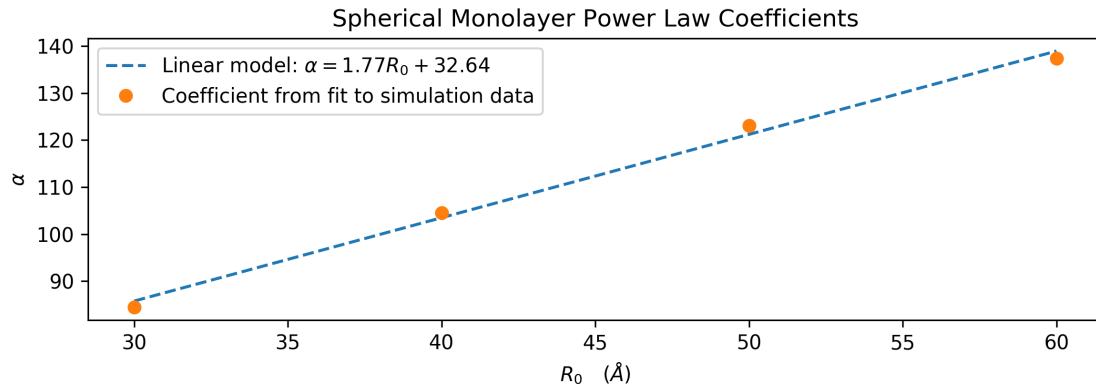
### 3.3.2 Cylindrical
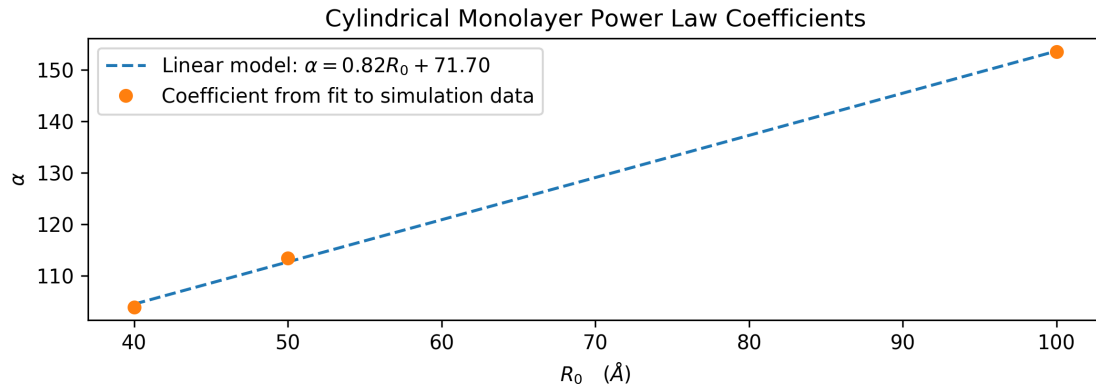


Figure 3.14: Droplet size dependence of $\alpha$ for cylindrical droplets from $r_m(t) = \alpha t^\beta$, with $\beta = 0.25$.
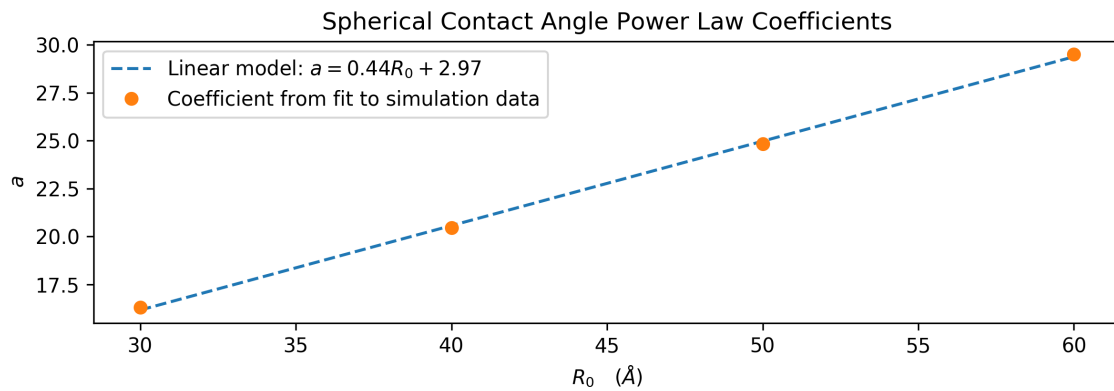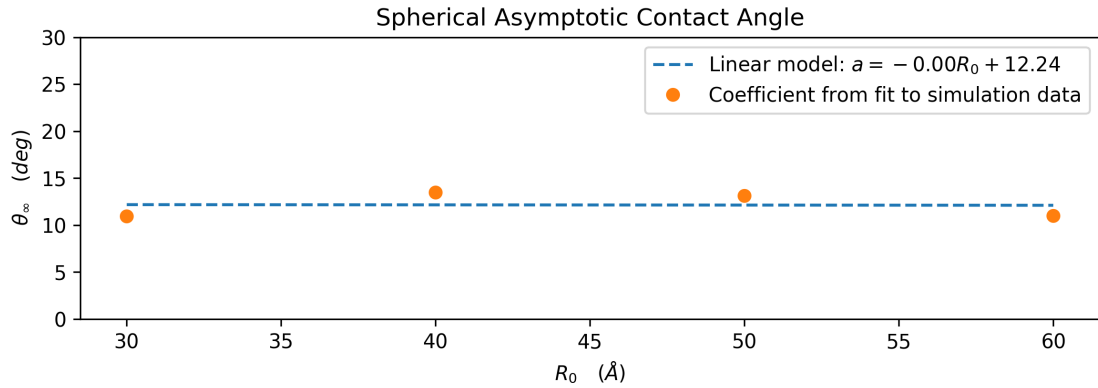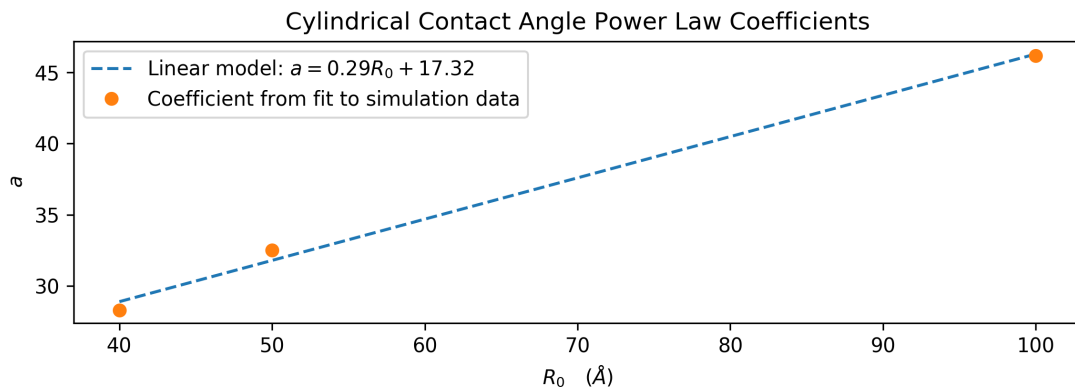


Figure 3.15: Droplet size dependence of $a$ for cylindrical droplets from $r_m(t) = at^b$, with $\beta = 0.25$.

| Droplet Size | $\alpha$ | $a$ |
|---|---|---|
| 40Å | 103.90 | 28.31 |
| 50Å | 113.36 | 32.50 |
| 100Å | 153.53 | 46.15 |

$$\alpha^{\mathrm{cyl}} = 0.82R_0 + 71.70 \tag{3.8}$$

$$a^{\mathrm{cyl}} = 0.29R_0 + 17.32 \tag{3.9}$$

Table 3.2: Cylindrical fit coefficients

## 3.4   Comparison with Previous Work

We briefly discuss how the results of these simulations compare to other published results in the literature. In [9], the authors simulate cylindrical droplets of Pb(1) and $N = 10$ polymers on a Cu(111) surface. They observe $r_m \sim \sqrt{t}$, whereas our simulations show $r_m \sim t^{1/4}$. They also show that $r_m \sim R_0^{4/5}$. This matches our own Equation 3.8 quite well.

The most important difference we observe in this work, however, is that the bulk radius does not increase monotonically, but rather decreases after achieving a maximum value. Several studies in the literature [9, 4, 6, 5] give descriptions of how the bulk radius increases, but nowhere have we found mention in the literature of a decreasing bulk radius in a spreading droplet.

CHAPTER IV

MATHEMATICAL MODEL

We now construct a mathematical model consisting of ordinary differential equations which allows for the computation of $r_b$ and $h_b$. We combine the relationships observed in the simulated data in Section 3.1 and Section 3.2 with the assumption that mass is conserved within the droplet between the bulk and the monolayer. Although some evaporation does cause the mass of the droplet to decrease, the effect is negligible and mass conservation is a reasonable estimation. We further assume that the bulk is a perfect spherical cap with density and that the monolayer is a perfect cylinder, and that the water densities in the bulk and monolayer assume the values $\rho_b$ and $\rho_m$ respectively, and are constant over time and space.

4.1  Generic Droplet Geometry

A great deal of work is saved by writing down the conservation of mass equation not in terms of $r_b$ and $h_b$ directly, but rather in terms of $\theta$ and $R$, the radius of the full sphere of which the droplet's spherical cap is just a part. We will therefore derive the volume formulas for both types of droplets in terms of these quantities. The same approach is taken with both the spherical and cylindrical droplets with slight variations in the details. In both cases, the following conversions between $(\theta, R)$ and
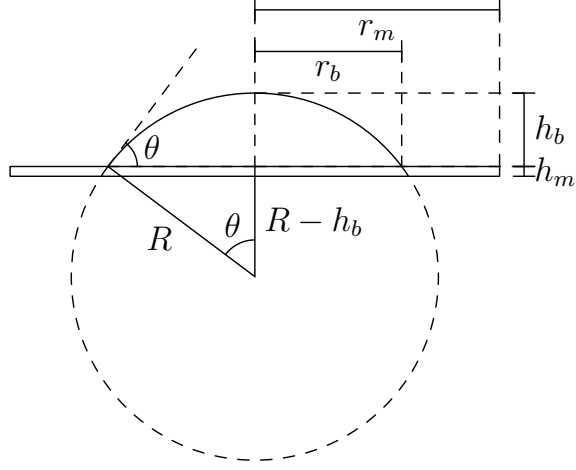
Figure 4.1: Generic circular droplet geometry

$(h_b, r_b)$ are valuable. From the figure, we see that

$$r_b = R \sin \theta, \tag{4.1}$$

$$h_b = R(1 - \cos \theta), \tag{4.2}$$

$$R^2 = (R - h_b)^2 + r_b^2. \tag{4.3}$$

Then, (4.3) and (4.2) respectively give

$$R = \frac{h_b^2 + r_b^2}{2h_b}, \tag{4.4}$$

$$\theta = \cos^{-1}\left(1 - \frac{h_b}{R}\right). \tag{4.5}$$

## 4.2 Spherical Model
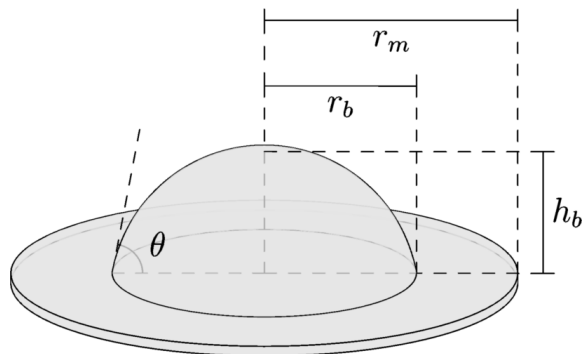


Figure 4.2: Spherical droplet geometry

For the spherical droplet, the monolayer is a thin cylinder, and its volume is given by

$$V_m = \pi r_m^2 h_m. \tag{4.6}$$

The bulk volume of the spherical droplet is calculated as follows, where $\eta$ is polar angle and $\gamma$ is azimuthal angle, to avoid confusion with the contact angle $\theta$. We also have $r_\eta = \cos\theta \sec\eta$ as the distance from the center of the sphere to the

bottom of the spherical cap as a function of $\eta$.

$$
\begin{aligned}
V_b &= \frac{2\pi}{3} \int_0^\theta \sin\eta\, r^3 \Big|_{R\cos\theta\sec\eta}^{R} d\eta \\
&= \frac{2\pi}{3} \int_0^\theta \sin\eta \left(R^3 - R^3\cos^3\theta\sec^3\eta\right) d\eta \\
&= \frac{2}{3}\pi R^3 \left[ \int_0^\theta \sin\eta\, d\eta - \cos^3\theta \int_0^\theta \tan\eta\sec^2\eta\, d\eta \right] \\
&= \frac{2}{3}\pi R^3 \left[ (1-\cos\theta) - \frac{1}{2}\cos^3\theta\tan^2\eta\Big|_0^\theta \right] \\
&= \frac{\pi R^3}{3}\left[2 - 2\cos\theta - \cos^3\theta\tan^2\theta\right] \\
&= \frac{\pi R^3}{3}\left[2 - 2\cos\theta - \cos\theta\sin^2\theta\right] \\
&= \frac{\pi R^3}{3}\left[2 + 3\cos\theta + \cos\theta\left(1 - \sin^2\theta\right)\right] \\
&= \frac{\pi R^3}{3}\left(2 + 3\cos\theta - \cos^3\theta\right).
\end{aligned}
$$

Then, the total mass of the droplet is

$$
\begin{aligned}
M &= \rho_b V_b + \rho_m V_m \\
&= \frac{\pi\rho_b}{3} R^3(2 - 3\cos\theta + \cos^3\theta) + \pi\rho_m r_m^2 h_m,
\end{aligned}
$$

and therefore

$$
\begin{aligned}
\dot{M} &= \frac{\pi\rho_b}{3}\left[3R^2\dot{R}(2 - 3\cos\theta + \cos^3\theta) + R^3(3\sin\theta - 3\cos^2\theta\sin\theta)\dot\theta\right] \\
&\quad + 2\pi\rho_m h_m r_m \dot{r}_m \\
&= \pi\rho_b\left[R^2\dot{R}(2 - 3\cos\theta + \cos^3\theta) + R^3\sin^3(\theta)\dot\theta\right] + 2\pi\rho_m h_m r_m \dot{r}_m.
\end{aligned}
$$

Let

$$
q = 2 - 3\cos\theta + \cos^3\theta. \tag{4.7}
$$

27

Then, enforcing $\dot{M} = 0$ gives

$$\dot{R}q + R\sin^3(\theta)\dot{\theta} + \frac{2\rho_m h_m r_m \dot{r}_m}{\rho_b R^2} = 0. \tag{4.8}$$

Then, the final equation for conservation of mass in the droplet system is

$$\dot{R} = -\frac{1}{q}\left[R\sin^3(\theta)\dot{\theta} + \frac{2\rho_m h_m r_m \dot{r}_m}{\rho_b R^2}\right]. \tag{4.9}$$

Recall that the following trends are observed in the simulation data

$$r_m(t) = \alpha t^\beta \tag{4.10}$$

$$\theta(t) = \theta_\infty + at^{-b}. \tag{4.11}$$

Differentiating gives

$$\dot{r}_m(t) = \alpha\beta t^{\beta-1} \tag{4.12}$$

$$\dot{\theta}(t) = -abt^{-b-1}, \tag{4.13}$$

which is sufficient information to solve (4.9) numerically using any standard finite difference method.

An initial time of $t = 0.1\,\mathrm{ns}$ is chosen to begin solving the ODE. Initial conditions are chosen by interpolating the fitting curves described in Chapter 3 to obtain $\theta(t_0)$ and $r_m(t_0)$. Then, $R(t_0)$ can be calculated using (4.4). Once (4.9) is solved numerically for $R$, we can calculate $r_b$ and $h_b$ using (4.1) and (4.2).
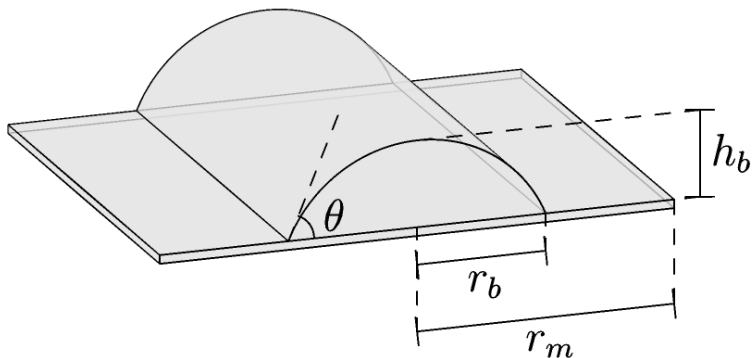
## 4.3 Cylindrical Model



Figure 4.3: Cylindrical droplet geometry

As before, we calculate the bulk volume and apply conservation of mass. Here, $L$ is an arbitrary length of the cylinder along its axis of symmetry.

$$
\begin{aligned}
V_b &= \int_0^L \int_{-\theta}^{\theta} \int_{r_\eta}^{R} r\, dr\, d\eta\, dz \\
&= L \int_0^{\theta} r^2 \Big|_{R\cos\theta\sec\eta}^{R}\, d\eta \\
&= R^2 L \int_0^{\theta} \left(1 - \cos^2\theta \sec^2\eta\right)\, d\eta \\
&= R^2 L \left(\theta - \cos^2\theta \int_0^{\theta} \sec^2\eta\, d\eta\right) \\
&= R^2 L \left(\theta - \cos^2\theta \tan\eta \Big|_0^{\theta}\right) \\
&= R^2 L \left(\theta - \sin\theta\cos\theta\right) \\
&= R^2 L \left(\theta - \frac{\sin(2\theta)}{2}\right).
\end{aligned}
$$

Then, the total mass is

$$M = \rho_b V_b + \rho_m V_m$$

$$= \rho_b R^2 L \left[ \theta - \frac{\sin(2\theta)}{2} \right] + 2\rho_m h_m L r_m,$$

and therefore

$$\dot{M} = 2\rho_b R \dot{R} L \left[ \theta - \frac{\sin(2\theta)}{2} \right]$$

$$+ \rho_b L R^2 \left[ \dot{\theta} - \cos(2\theta)\dot{\theta} \right] + 2\rho_m h_m L \dot{r}_m. \tag{4.14}$$

Then, requiring $\dot{M} = 0$ gives

$$\dot{R} = - \left[ \theta - \frac{\sin(2\theta)}{2} \right]^{-1} \left[ \frac{R\dot{\theta}}{2}(1 - \cos(2\theta)) + \frac{\rho_m h_m \dot{r}_m}{\rho_b R} \right],$$

which yields the conservation of mass equation for cylindrical droplets,

$$\dot{R} = - \left[ \theta - \frac{\sin(2\theta)}{2} \right]^{-1} \left[ R\dot{\theta} \sin^2 \theta + \frac{\rho_m h_m \dot{r}_m}{\rho_b R} \right]. \tag{4.15}$$

As before, we complement Equation 4.15 with observations from the data.

$$r_m(t) = \alpha t^\beta \tag{4.16}$$

$$\theta(t) = \theta_\infty + at^{-b}. \tag{4.17}$$

Hence,

$$\dot{r}_m(t) = \alpha\beta t^{\beta-1} \tag{4.18}$$

$$\dot{\theta}(t) = -abt^{-b-1}. \tag{4.19}$$

As in Section 4.2, initial conditions are chosen by interpolating fitting curves, and $r_b$ and $h_b$ are calculated from $R$ using (4.1) and (4.2).

30

## 4.4　Results

Values of $\rho_m = 1.5$ and $h_m = 1.75$ are found from the data in Section 2.2.3, although better visual agreement with the data is achieved by using $\rho_m = 1.85$ for the spherical droplets and $\rho_m = 2.1$ for the cylindrical droplets. Further work in tuning the model is necessary. The following plots are the result of solving the model described in Sections 4.2 and 4.3 numerically using the ODE solver in Python's SciPy package [10].
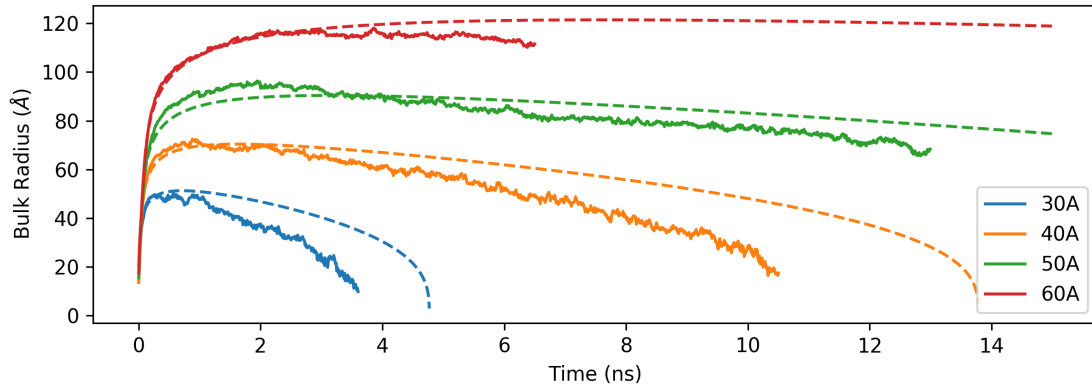
Figure 4.4: Spherical model $r_b$ results compared to data with $\rho_m = 1.5$, $h_m = 1.75$, as calculated in Section 2.2.3.
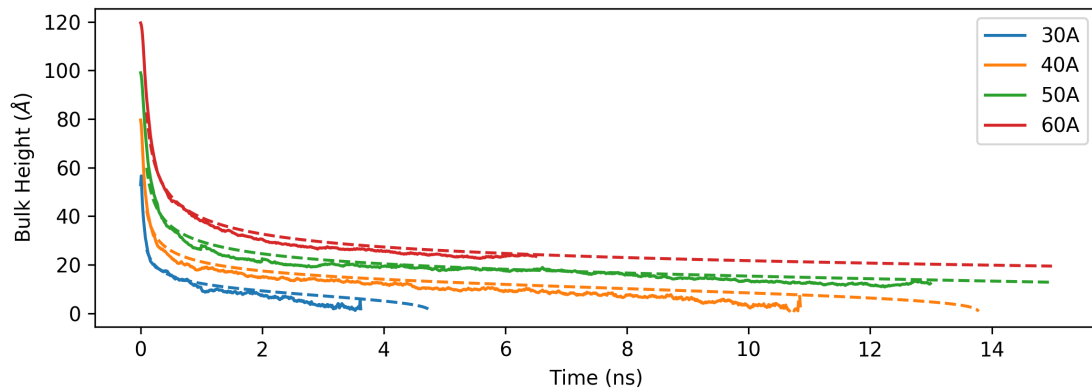


Figure 4.5: Spherical model $h_b$ results compared to data with $\rho_m = 1.5$, $h_m = 1.75$, as calculated in Section 2.2.3.
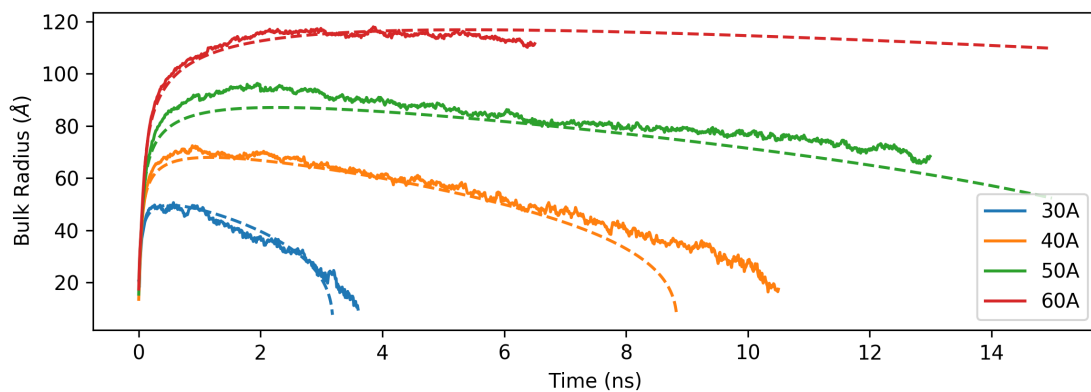
Figure 4.6: Spherical model $r_b$ results compared to data with $\rho_m = 1.85$, $h_m = 1.75$, tweaked to better match data visually.
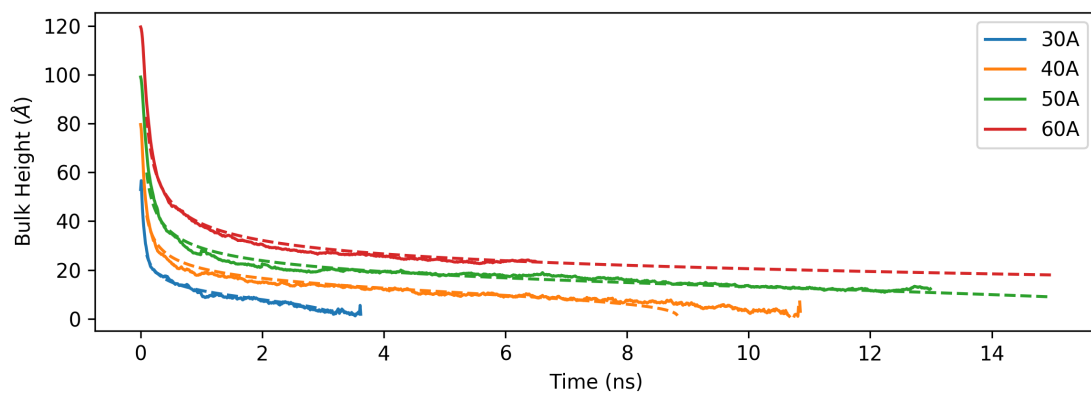


Figure 4.7: Spherical model $h_b$ results compared to data with $\rho_m = 1.85$, $h_m = 1.75$, tweaked to better match data visually.

Figure 4.8: Cylindrical model $r_b$ results compared to data with $\rho_m = 1.5$, $h_m = 1.75$, as calculated in 2.2.3.

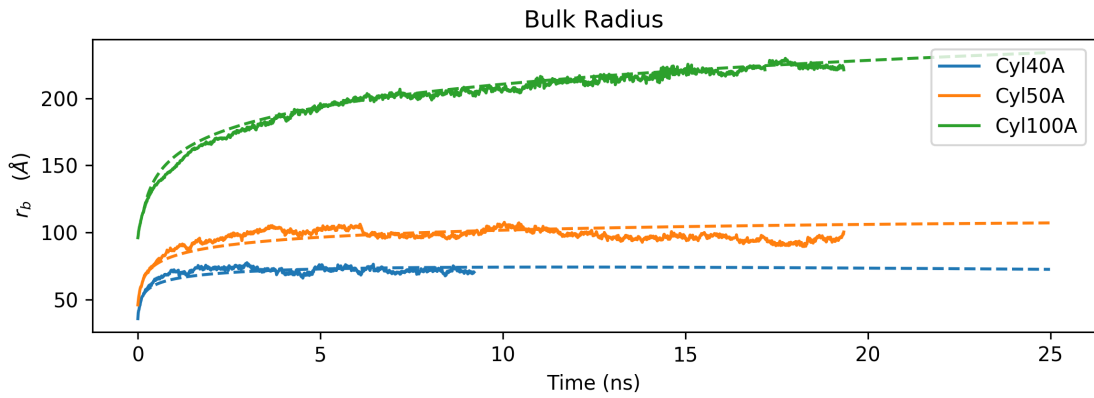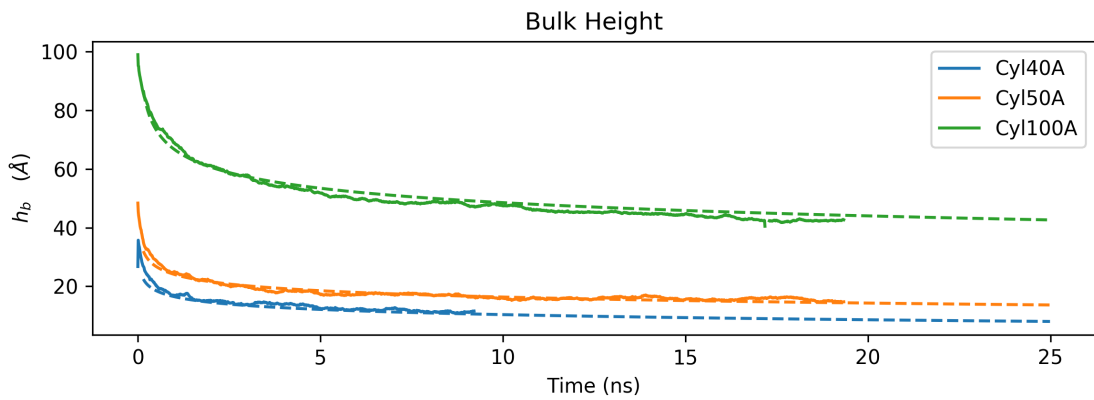

Figure 4.9: Cylindrical model $h_b$ results compared to data with $\rho_m = 1.5$, $h_m = 1.75$, as calculated in 2.2.3.
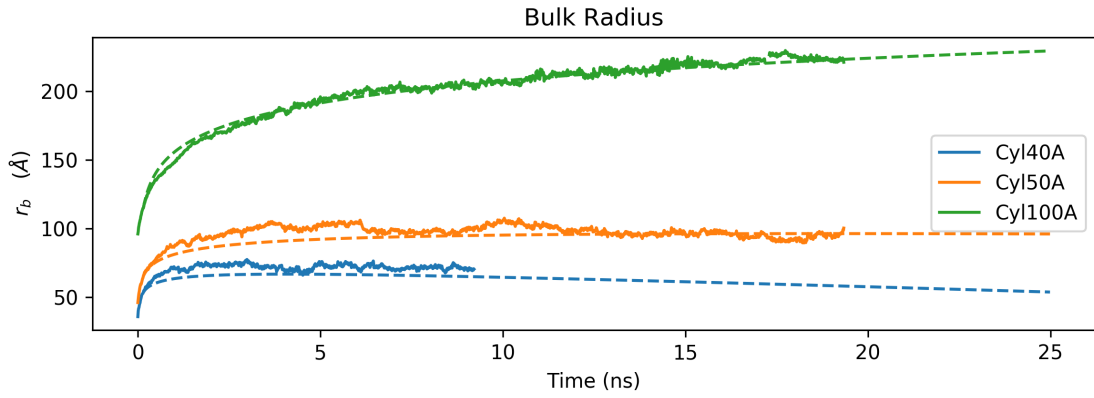
Figure 4.10: Cylindrical model $r_b$ results compared to data with $\rho_m = 2.1$, $h_m = 1.75$, tweaked to better match data visually.
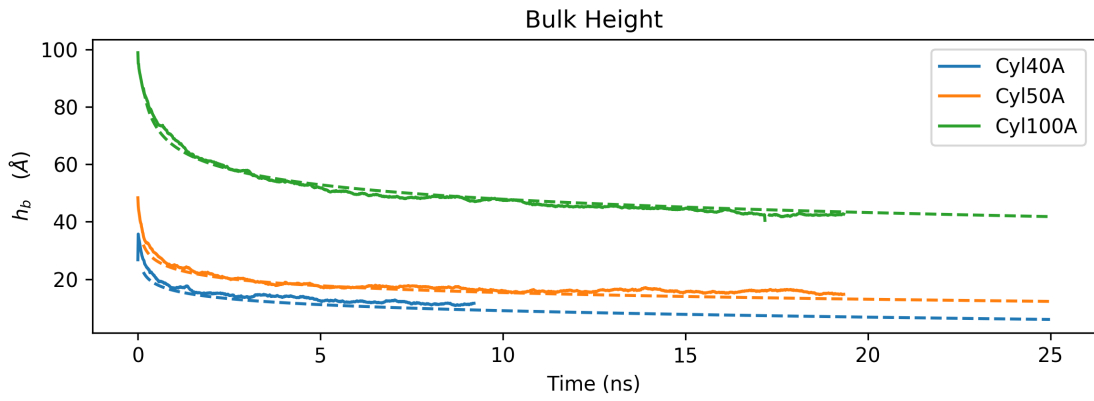


Figure 4.11: Cylindrical model $r_m$ results compared to data with $\rho_m = 2.1$, $h_m = 1.75$, tweaked to better match data visually.

CHAPTER V

CONCLUSION

We have observed through molecular dynamics simulation a novel phenomenon previously unobserved in the literature; namely, that the bulk radius of nanoscopic spherical water droplets is non-monotonic and obtains a single global maximum. We observe that the spherical droplets maintain a nonzero contact angle until the final moments of wetting. Our results are less conclusive for cylindrical water droplets, and more computational time is presently being dedicated to their simulation. We find that cylindrical droplets require significantly longer timescales to undergo complete wetting. While a $40\,\text{Å}$ spherical droplet fully wets the sapphire surface in $10\,\text{ns}$, we estimate that a $40\,\text{Å}$ cylindrical droplet may take up to $100\,\text{ns}$.

We find clear trends in the data which describe the time evolution of the monolayer radius and of the contact angle as power laws, and we present a simple mathematical model based on conservation of mass to predict the bulk radius and droplet height. We find different results for the time dependence of the monolayer radius than those found in the literature, but similar droplet size dependence. By using simple linear relationships among the power law parameters, it is possible to use the model to predict the geometrical aspect of wetting dynamics for droplet sizes which have not yet been treated via all-atom simulation.

# BIBLIOGRAPHY

[1] H. J. C. Berendsen, J. R. Grigera, and T. P. Straatsma. The missing term in effective pair potentials. *Journal of Physical Chemistry*, 91(24):6269–6271, Aug. 1987.

[2] T. D. Blake and T. U. K. *The Physics of Moving Wetting Lines*.

[3] R. T. Cygan, J.-J. Liang, and A. G. Kalinichev. Molecular Models of Hydroxide, Oxyhydroxide, and Clay Phases and the Development of a General Force Field. *Journal of Physical Chemistry*, 108(4):1255–1266, Nov. 2003.

[4] J. De Coninck, U. D'Ortona, J. Koplik, and J. R. Banavar. Terraced Spreading of Chain Molecules via Molecular Dynamics. *Physical Review Letters*, 74(6):928–931, Feb. 1995.

[5] P. G. de Gennes. Wetting: statics and dynamics. *Reviews of Modern Physics*, 57(3), July 1985.

[6] M. J. de Ruijter, T. D. Blake, and J. De Coninck. Dynamic Wetting Studied by Molecular Modeling Simulations of Droplet Spreading. *Langmuir*, 15(22):7836–7847, Oct. 1999.

[7] Gerhardus Koch, Jeff Varney, Neil Thompson, Oliver Moghissi, Melissa Gould, and Joe Payer. International Measures of Prevention, Application, and Economics of Corrosion Technologies Study. Technical report, NACE International, Houston, Texas, 2016.

[8] J. D. Halverson, C. Maldarelli, A. Couzis, and J. Koplik. Wetting of hydrophobic substrates by nanodroplets of aqueous trisiloxane and alkyl polyethoxylate surfactant solutions. *Chemical Engineering Science*, page 11, 2009.

[9] D. R. Heine, G. S. Grest, and E. B. Webb. Surface Wetting of Liquid Nanodroplets: Droplet-Size Effects. *Physical Review Letters*, 95(10), Aug. 2005.

[10] E. Jones, T. Oliphant, P. Peterson, and others. SciPy: Open source scientific tools for Python, 2001.

[11] O. Parent. Anti-icing and de-icing techniques for wind turbines: Critical review. *Cold Regions Science and Technology*, page 9, 2011.

[12] S. Plimpton. Fast Parallel Algorithms for ShortRange Molecular Dynamics. *Journal of Computational Physics*, 117:1–19, Mar. 1995.

[13] G. Scocchi, D. Sergi, C. DAngelo, and A. Ortona. Wetting and contact-line effects for spherical and cylindrical droplets on graphene layers: A comparative molecular-dynamics investigation. *PHYSICAL REVIEW E*, page 8, 2011.

[14] S. J. Weinstein and a. K. J. Ruschak. Coating Flows. *Annual Review of Fluid Mechanics*, 36(1):29–53, 2004.

[15] L. Zhou, H.-J. Xu, S.-K. Gong, and D.-W. Li. Research of Aircraft Icing Characteristics and Anti-icing and De-icing Technology. *Zhongguo Anquan Kexue Xuebao / China Safety Science Journal*, 20(6):105–110, 2010.